HHS Public Access

Author manuscript

Nat Genet. Author manuscript; available in PMC 2017 June 12.

Published in final edited form as:

Nat Genet. 2017 February ; 49(2): 289–295. doi:10.1038/ng.3746.

SMARCB1-mediated SWI/SNF complex function is essential for enhancer regulation

Xiaofeng Wang[1,2,3,*], **Ryan S. Lee**[1,2,3,*], **Burak H. Alver**[4,*], **Jeffrey R. Haswell**[1,2,3], **Su Wang**[4], **Jakub Mieczkowski**[5], **Yotam Drier**[6,7], **Shawn M. Gillespie**[6,7], **Tenley C. Archer**[8], **Jennifer N. Wu**[1,2,3], **Evgeni P. Tzvetkov**[1,2,3], **Emma C. Troisi**[1,2,3], **Scott L. Pomeroy**[8], **Jaclyn A. Biegel**[9], **Michael Y. Tolstorukov**[5], **Bradley E. Bernstein**[6,7,10,#], **Peter J. Park**[4,11,#], and **Charles W. M. Roberts**[1,2,3,12,#]

[1]Department of Pediatric Oncology, Dana-Farber Cancer Institute, Boston, MA 02215, USA

[2]Division of Hematology/Oncology, Boston Children's Hospital, MA 02215, USA

[3]Department of Pediatrics, Harvard Medical School, Boston MA 02215, USA

[4]Department of Biomedical Informatics, Harvard Medical School, Boston, MA 02115, USA

[5]Department of Molecular Biology, Massachusetts General Hospital, Boston, Massachusetts 02114, USA

[6]Department of Pathology and Center for Cancer Research, Massachusetts General Hospital and Harvard Medical School, Boston, MA 02114, USA

[7]Broad Institute of MIT and Harvard, Cambridge, MA 02142, USA

[8]Department of Neurology, Boston Children's Hospital, Harvard Medical School, Boston, MA 02215, USA

[9]Department of Pathology and Laboratory Medicine, Children's Hospital Los Angeles and Keck School of Medicine at University of Southern California, Los Angeles, CA 90033, USA

[10]Howard Hughes Medical Institute, Chevy Chase, MD 20815, USA

[11]Division of Genetics, Brigham and Women's Hospital, Boston, MA 02115, USA

[12]Comprehensive Cancer Center and Department of Oncology, St. Jude Children's Research Hospital, Memphis, TN 38105, USA

*Co-first author

#Co-senior author

Accession codes

All sequencing data have been submitted to the GEO database (http://www.ncbi.nlm.nih.gov/geo/) with accession number GSE71506.

Author Contributions

X.W., R.S.L., B.H.A., B.E.B., P.J.P., and C.W.R. conceived experiments and study design. X.W., J.R.H., E.P.T. and E.C.T. performed all cell line experiments. R.S.L. and S.M.G. performed all primary tumor experiments. B.H.A., R.S.L., S.W., J.M., and Y.D. performed computational analyses of the data. X.W., R.S.L., B.H.A. and S.W. performed statistical analyses. T.C.A., S.L.P., and J.A.B. contributed primary tumor samples and clinical data. J.N.W. designed SMARCB1 re-expression vector. X.W., R.S.L., B.H.A., J.R.H., J.M., Y.D., M.Y.T., B.E.B., P.J.P., and C.W.R. contributed to the interpretation of experiments. X.W., R.S.L, B.H.A., and C.W.R. wrote the manuscript with input from all co-authors.

Abstract

SMARCB1 (SNF5/INI1/BAF47), a core subunit of the SWI/SNF (BAF) chromatin remodeling complex[1,2], is inactivated in nearly all pediatric rhabdoid tumors[3–5]. These aggressive cancers are among the most genomically stable[6–8], suggesting an epigenetic mechanism by which SMARCB1 loss drives transformation. Here, we show that despite indistinguishable mutational landscapes, human rhabdoid tumors show distinct enhancer H3K27ac signatures, which reveal remnants of differentiation programs. We show that SMARCB1 is required for the integrity of SWI/SNF complexes and that its loss alters enhancer targeting – markedly impairing SWI/SNF binding to typical enhancers, particularly those required for differentiation, while maintaining SWI/SNF binding at super-enhancers. We show that these retained super-enhancers are essential for rhabdoid tumor survival, including some that are shared across all subtypes, such as *SPRY1*, and other lineage-specific super-enhancers, like *SOX2* in brain-derived rhabdoid tumors. Taken together, our findings reveal a novel chromatin-based epigenetic mechanism underlying the tumor suppressive activity of SMARCB1.

The loss of SMARCB1 (SNF5/INI1/BAF47) is the sole driving genetic event that characterizes rhabdoid tumors, which arise in the brain, kidney, and soft tissues[5,9]. Given their highly malignant behavior, in spite of remarkably simple genomes, we sought to understand how a mutated chromatin regulator might deregulate transcription to drive oncogenesis. We began by characterizing the chromatin landscape of rhabdoid tumors by examining histone modifications in 12 tissue samples and three cell lines from rhabdoid tumors of different tissues (Supplementary Fig. 1a). Most had been exome-sequenced and are characterized by very low mutation rates and a high degree of purity[6]. Using chromatin immunoprecipitation followed by sequencing (ChIP-seq), we profiled genome-wide enrichment of three key histone modifications – H3K4me3, H3K4me1, and H3K27ac – to define *cis*-regulatory promoter and enhancer elements[10]. We identified putative active promoters as transcription start site (TSS)-proximal loci containing H3K27ac and H3K4me3 signal and putative enhancers as TSS-distal (>2kb away from active TSS) loci containing H3K27ac but not H3K4me3 signal. In Fig. 1a–c, we show the Pearson correlation coefficients for the three histone marks, among primary tumors, three rhabdoid cell lines, and normal tissues (adult brain, kidney, and others from the NIH Roadmap Epigenomics Project[11,12]). Compared to H3K4me3 at promoters, H3K4me1 at enhancers revealed more variability, although tumors, whether primary or cell lines, showed higher within-group correlation (Fig. 1a–b, Supplementary Fig. 1b–c). Importantly, evaluation of H3K27ac at enhancers revealed distinct profiles for each tumor (Fig. 1c, Supplementary Fig. 1d), except for moderate correlation amongst some brain-derived or some kidney-derived samples. The presence of subpopulations in brain or kidney rhabdoid tumors is consistent with recent findings based on gene expression and DNA methylation[13,14]. This suggests that despite their low mutation rate genomes, rhabdoid tumors contain substantial variation within the chromatin landscape at enhancers.

Given the much greater variation at enhancers relative to promoters, we focused on enhancers and sought to identify potential enhancer target genes and pathways specific to each subpopulation. K-means clustering based on H3K27ac signals at enhancer peaks revealed clusters characteristic of rhabdoid tumors from each of the different tissues of

origin, as well as a cluster of shared enhancers (Fig. 1d). To analyze the potential role of these enhancer clusters, each enhancer was assigned to the nearest TSS within the same conserved CTCF regulatory boundaries[15]. Gene ontology (GO) analysis performed on the different clusters revealed that brain-derived rhabdoid tumors were enriched for active enhancers near neurogenesis genes (Fig. 1e and Supplementary Table 1), while kidney-derived rhabdoid tumors were enriched for terms such as wound healing – a proliferative process thought to involve mesenchymal stem cells[16]. A few enhancers were shared across all samples and were enriched for genes associated with developmental processes. Collectively, these findings demonstrate that many enhancers found in rhabdoid tumors are associated with development and that lineage-specific enhancers are present in rhabdoid tumors from different tissues.

Super-enhancers – large clusters of enhancers with high cumulative H3K27ac levels[17,18] – have recently been implicated as controlling genes central to maintaining cell identity and, in cancer, genes underlying the malignant state[17,18]. Using H3K27ac signal to identify super-enhancers, we found a mean of 565 super-enhancers (SD=123) per primary sample and associated these super-enhancers with genes using the same method above. We found that super-enhancers specific to brain-derived tumors were near key regulators of neural development, such as *SOX2*[19], *FZD1/3*[20], and others (Fig. 1f and Supplementary Table 2). The kidney-derived tumors contained fewer super-enhancers that were specific to the kidney-derived samples, but included a super-enhancer proximal to *TBX2*, a regulator of kidney and other organ development[21]. As with all enhancers, these super-enhancers suggest that the persisting shadow of lineage specificity can still be found.

Because of the greatest differences seen in the primary tissues lied at putative enhancers, we next evaluated whether the loss of SMARCB1 directly contributes to these different TSS-distal H3K27ac signatures. Since we previously identified the dependence of rhabdoid tumors on SMARCA4 (BRG1)[22], suggesting the existence of an essential residual SWI/SNF complex despite the absence of SMARCB1, we sought to evaluate the function of this residual complex on the chromatin landscape. To do so, we established a doxycycline-inducible *SMARCB1* expression system.

We first evaluated the contribution of SMARCB1 in forming the SWI/SNF complex. In both G401 (kidney) and BT16 (brain) rhabdoid cell lines, *SMARCB1* re-expression resulted in significantly increased protein levels of numerous SWI/SNF subunits, particularly the tumor suppressor subunits ARID1A and ARID1B, as well as a marked increase in subunit incorporation into SWI/SNF complexes as shown by the immunoprecipitation (IP) of SMARCC1 (BAF155), SMARCA4, and ARID1A (Fig. 2a–b). There was no change in the mRNA expression of these subunits, and MG132 treatment increased the protein levels of some subunits, indicating that these changes are the result of post-translational regulation (Supplementary Fig. 2a–b). Similar effects were also observed in TM87 and A204 soft tissue-derived rhabdoid cell lines (Supplementary Fig. 2c–d). In contrast, induction of exogenous *SMARCB1* in the control *SMARCB1*-wildtype ES2 ovarian cancer cell line had no effect (Supplementary Fig. 2e). Furthermore, IP of SMARCC1 or SMARCA4 followed by mass spectrometry revealed that re-expression of *SMARCB1* resulted in significantly more peptides corresponding to SWI/SNF subunits (Fig. 2c, Supplementary Fig 2f and

Supplementary Table 3). To directly evaluate the effect of *SMARCB1* re-expression upon SWI/SNF complex integrity, we next performed a glycerol sedimentation assay in G401 and BT16 cells. An intact residual SWI/SNF complex was only faintly detectable prior to re-expression of *SMARCB1* (Fig. 2d and Supplementary Fig. 2g). However, upon re-expression, we observed markedly increased levels of SWI/SNF complex. Conversely, to evaluate the effect of SMARCB1 loss in normal cells, we used *Smarcb1*$^{fl/fl}$ mouse embryonic fibroblasts[23]. *Smarcb1* deletion resulted in substantially reduced protein levels of several SWI/SNF subunits, including ARID1A and ARID1B, and reduced subunit incorporation into the complex without concomitant changes in mRNA levels (Fig. 2e and Supplementary Fig. 2h). These biochemical studies demonstrate that SMARCB1 is essential for SWI/SNF complex stability, particularly for ARID1A, the most frequently mutated SWI/SNF subunit in cancer.

We next investigated how this alteration in SWI/SNF complex composition and abundance affects complex targeting and binding. We performed ChIP-seq of the core SWI/SNF subunits SMARCA4 and SMARCC1 in the G401, BT16, and TTC549 rhabdoid lines for which we had also profiled histone marks (Supplementary Fig. 1a), before and after *SMARCB1* induction. *SMARCB1* expression led to a substantial increase in SMARCA4 and SMARCC1 binding, which were themselves highly correlated, with many more binding sites gained than lost (Fig. 3a–b and Supplementary Fig. 3a–c, 4a–b, 5a-b). While SWI/SNF's role of organizing nucleosomes at promoters has been established[24], we observed that the majority of SWI/SNF binding actually occurs instead at TSS-distal enhancers marked with H3K4me1 and/or H3K27ac (Fig. 3a, Supplementary Fig. 4a and 5a), consistent with recent reports showing SMARCA4 enhancer binding[25–27]. As was the case in the absence of SMARCB1, the majority of SWI/SNF targeting was gained at TSS-distal sites (Fig. 3a–b). Thus, with or without SMARCB1, the SWI/SNF complex targets predominantly to TSS-distal sites, with the number of sites markedly increased in the presence of SMARCB1.

To investigate a link between SMARCB1 and enhancer regulation, we categorized TSS-distal SWI/SNF targets based on their sensitivity to *SMARCB1* re-expression, as lost (> 1.5-fold reduction), gained (> 1.5-fold gain), or unchanged sites. At the gained sites, we also observed increased enhancer-associated H3K27ac and H3K4me1flanking the peak SWI/SNF binding positions (Fig. 3c–d, Supplementary Fig. 4c–d, 5c–d). Conversely, the few lost sites showed a decrease in H3K27ac levels. These findings reveal SWI/SNF as preferentially active at enhancers and establish a direct role for SMARCB1 in establishing the active chromatin landscape at enhancers.

To investigate the biological relevance of SMARCB1 to enhancer function, we performed RNA-seq on six rhabdoid cell lines, including those above, before and after *SMARCB1* re-expression. Significantly more genes were upregulated than downregulated in all lines (Supplementary Fig. 6), and the changes correlated with nearby TSS-distal SWI/SNF binding and enhancer changes (Fig. 3e, Supplementary Fig. 4e and 5e). In contrast to a prior report that SMARCB1 was dispensable for the control of a handful of SMARCA4-dependent genes[28], our results demonstrate that SMARCB1 loss affects a large majority of SWI/SNF regulated genes. To gain insight into the effects of SMARCB1-mediated enhancer induction, we performed GO enrichment analysis for genes near enhancers with increased

SWI/SNF binding, relative to any enhancer-proximal genes (See Methods). For all three cell types, the identified GO terms were particularly associated with development and differentiation. Cell-type specific GO terms were also observed, such as morphogenesis of branching epithelium in kidney rhabdoid-derived G401 cells and neuron differentiation in brain rhabdoid-derived BT16 cells (Fig. 3f, Supplementary Fig. 4f, 5f and Supplementary Table 4). Consistent with a shared mechanistic basis, however, both GO analysis and gene set enrichment analysis (GSEA) of differentially expressed genes across all cell lines revealed commonly shared terms including developmental process, cell differentiation, and SMARCE1 targets (Supplementary Fig. 6 and 7). Collectively, these findings demonstrate that *SMARCB1* re-expression results in increased SWI/SNF complex enrichment at enhancers, particularly those related to development and differentiation, in gained chromatin marks reflective of an active state, and in upregulated expression of genes associated with tissue-specific differentiation.

Having identified a role for SMARCB1 in the control of enhancer formation and function, we next asked whether SMARCB1 contributes to super-enhancer formation and function. Because of their distinct structure, the concentration of constituent proteins required to maintain super-enhancer integrity has been shown to differ substantially from that required to maintain the integrity of regular enhancers[29]. Unlike the effect upon typical enhancers, we did not observe significant changes in the number or position of super-enhancers upon *SMARCB1* re-expression (Supplementary Fig. 8a–c). Even without SMARCB1, the SWI/SNF complex was already bound at super-enhancers (Fig. 4a–c and Supplementary Fig. 9a–b). *SMARCB1* re-expression facilitated only a modest increase in SWI/SNF binding at super-enhancers, and this had no effect on the levels of H3K27ac or H3K4me1 (Fig. 4a–b and Supplementary Fig. 9a–d). This observation suggests differential functions for SMARCB1 at regular enhancers compared to super-enhancers – it serves a role in the activation of differentiation-related regular enhancers but it is largely dispensable for super-enhancers (Fig. 4b–c). We confirmed the residual complex binding at super-enhancers by performing ChIP-qPCR (Supplementary Fig 10) and found that further reduction of SWI/SNF via knockdown of either SMARCC1 or SMARCD1 resulted in reduced residual complex binding at the super-enhancer accompanied by reduced gene expression (Supplementary Fig 10). The preferential targeting of the residual complex to super-enhancers may be due to a higher density of transcriptional co-regulators at super-enhancers that results in higher affinity and greater stability of the SWI/SNF complex compared to typical enhancers.

Given that the mutational burden is similarly low among rhabdoid tumors from different tissues, we reasoned that super-enhancers shared across rhabdoid tumors from different organs might be associated with genes essential for survival. To define this set of shared super-enhancers, we identified those that (1) overlapped with the most commonly shared enhancers found in bottommost cluster of Figure 1d, (2) were also identified in all three rhabdoid tumor cell lines, and (3) were not found in normal tissues. Among the 10 super-enhancers matching these criteria were ones proximal to *SPRY1*, *SALL4,* and *HMGA2* (Supplementary Fig. 11a–c). Interestingly, *HMGA2* has previously been implicated in rhabdoid tumor proliferation[30]. We found that *SALL4* and *SPRY1* are also essential for rhabdoid tumor proliferation, as shRNA knockdown of either of these genes significantly

impaired the proliferation of all three cell lines tested (Fig. 4d–f). Meanwhile, as mentioned above, we found that the *SOX2*-associated super-enhancer is brain rhabdoid-specific (Supplementary Fig. 11d), suggesting that these tissue-specific super-enhancers could also be essential for the survival of these cancers. Consistent with this, shRNA-mediated knockdown of *SOX2* specifically impaired the proliferation of BT16, but has no effect on G401 (Fig. 4f–g).

Taken together, our findings present a mechanistic framework for the function of SMARCB1 in the control of cell identity and the mechanism by which mutation of this core SWI/SNF subunit drives cancer formation (Fig. 5): SMARCB1 functions to stabilize the SWI/SNF complex, enabling it to bind and facilitate enhancer formation and function. SMARCB1 loss results in a marked reduction in the amount of SWI/SNF complexes, to levels that are unable to maintain normal enhancer function. The small amount of residual SWI/SNF complex that remains is preferentially bound to super-enhancers. It is notable that while activation of regular enhancers is essential for differentiation, super-enhancers have been implicated in the maintenance of current cell identity. It is of further note that despite the extremely rapid cancer onset caused by *Smarcb1* inactivation in mice, only extremely specific cell types are susceptible to transformation[31], while the vast majority of cell types undergo arrest following SMARCB1 loss. Similarly, the spectrum of cancers associated with SMARCB1 loss in humans is quite specific. These findings collectively suggest a model in which loss of SMARCB1 impairs the function of enhancers, which are required for differentiation, whereas super-enhancers that underlie the current cell state are largely unaffected. In specific proliferative progenitor cell types, then, the consequence of reduced enhancer function with super-enhancer preservation may be to drive oncogenic transformation by locking cells in a poorly differentiated and highly proliferative state. Collectively, our work provides key insights into the mechanisms by which SWI/SNF subunit mutations cause cancer through impairment of enhancer function, and supports super-enhancer specified genes as essential in these cancers, thus revealing potential therapeutic targets.

Online Methods

Human primary tumor samples

Primary human tumor samples were collected and flash frozen. Tumors were reviewed to confirm the diagnosis and to estimate tumor content (Children's Hospital of Philadelphia, Boston Children's Hospital). All tumors have previously been exome sequenced[5]. Patients' guardians provided informed consent prior to their participation. Local IRBs (CHOP, BCH) approved collection and testing of each sample. Tissue was mechanically macerated while frozen and suspended in PBS with protease inhibitor.

Cell culture

G401, G402, A204, and ES-2 cell lines were purchased from American Type Culture Collection. BT12, BT16, TM87-16, and TTC549 cells were maintained in the lab. All cells have been tested negative for mycoplasma contamination. G401 and BT16 cells were cultured in DMEM with 10% FBS; G402, TM87-16, and ES-2 cells were cultured in McCoy's with 10% FBS; TTC549 cells were cultured in RPMI with 10% FBS; BT12 cells

were cultured in OptiMEM (Life Technologies) with 5% FBS at 37°C with 5% CO2. Mouse embryonic fibroblasts (MEFs) were generated as described previously[32]. To establish SMARCB1 inducible re-expression stable cell lines, cells were transduced with lentiviral pInducer-21-SMARCB1. 72 hours post transduction GFP+ cells were sorted and maintained in media with Tet-System Approved FBS (Clonetech, Cat. #631106). To induce SMARCB1 re-expression, cells were treated with doxycycline (1 μg/ml, EMD Millipore) for indicated time. For shRNA-mediated knockdown, cells were transduced with lentiviral shRNAs and selected with puromycin for 72 h before seeding for MTT or colony formation assays. MTT assays were conducted with an MTT Cell Proliferation Kit (Roche Diagnostics, Cat. #11465007001). Colony formation assays were conducted by staining cells for 20 min with crystal violet staining solution (0.05% crystal violet, 1% formaldehyde, 1% PBS, 1% methanol).

SALL4 (TRCN0000433893, TRCN0000419286, and TRCN0000021874), SPRY1 (TRCN0000344734, TRCN0000369465, and TRCN0000344733) shRNAs were obtained from the RNA interference (RNAi) screening core facility at the Dana-Farber Cancer Institute, SOX2 shRNA were purchase from GE Healthcare (V2LHS_153337, V3LHS_404430, V3LHS_404432) and were lentivirally transduced into G401, TTC549 and BT16 cells. Non-silencing control shRNA is in the pLKO.1 lentiviral expression vector backbone[32].

Co-immunoprecipitation and mass spectrometry

Nuclear extracts for co-immunoprecipitation were prepared using the NE-PER Nuclear and Cytoplasmic Extraction Kit (Thermo Scientific, Cat. #78835). Nuclear extracts were diluted with RIPA buffer (150 mM NaCl, 50 mM Tris-HCl pH 7.5, 1% Nonidet P-40, 0.5% sodium deoxycholate, 0.1% SDS, 1 mM DTT) to a final concentration of 1 mg/ml (with protease inhibitor cocktails, Roche). Each IP was incubated with antibodies overnight at 4°C. Protein G Dynabeads (Life Technologies, Cat. #10009D) were added and incubated at 4°C for 3 h. Beads were then washed three times with RIPA buffer and resuspended in reducing SDS gel loading buffer. Antibodies to the following proteins were used in the immunoprecipitation and immunoblots: SMARCC1/BAF155 (Santa Cruz: sc9746); ARID1A (Santa Cruz: sc-32761 for immunoprecipitation; Cell Signaling Technology: 12354 for immunoblotting); ARID1B (Abcam: ab54761); SMARCA4/BRG1 (Santa Cruz: sc17796); SMARCC2/BAF170 (Bethyl Laboratories: A301-039A); SMARCD1/BAF60A (Bethyl Laboratories: A301-595A); SMARCE1/BAF57 (Bethyl Laboratories: A300-810A); SMARCB1/SNF5 (Bethyl Laboratories: A301-087A); ACTL6A/BAF53A (Bethyl Laboratories: A301-391A); ACTIN (Cell Signaling Technology: 5125).

For mass spectrometry, equal amount of nuclear extract was used for each IP. Samples after IP were separated on a NUPAGE 12% Bis-Tris gel, and stained with SimplyBlue SafeStain (Life Technologies). Per IP sample, the whole lane was cut and sent for protein identification at the Taplin Mass Spectrometry Facility of Harvard Medical School.

Glycerol sedimentation assay

Nuclear fraction for sedimentation assay was prepared according to previous literatures (REF). Briefly, cells were harvested at indicated time points, then lysed and homogenized in Buffer A (10 mM HEPES (pH 7.6), 25 mM KCl, 1 mM EDTA, 10% glycerol, 1 mM DTT, and protease inhibitors (complete tablets, Roche) supplemented with 1 mM PMSF) on ice. Nuclei were sedimented by centrifugation (1,000 × g for 10 min), resuspended in Buffer B (10 mM HEPES (pH 7.6), 3 mM $MgCl_2$, 100 mM KCl, 0.1 mM EDTA, 10% glycerol, 1 mM DTT, and protease inhibitors), and further lysed by the addition of ammonium sulfate to a final concentration of 0.3 M. Soluble nuclear proteins were separated by the insoluble chromatin fraction by ultracentrifugation (100,000 × g for 20 min) and precipitated with 0.3 mg/ml ammonium sulfate for 20 min on ice. Protein precipitate was isolated by ultracentrifugation (100,000 × g for 30 min) and resuspended in Buffer A without glycerol. 1 mg of nuclear extract was carefully overlaid onto a 12-ml 10–30% glycerol (in RIPA buffer) gradient prepared in a 14-ml 14 × 95 mm polyallomer centrifuge tube (Beckman Coulter, Cat. #331374). Tubes were placed in an SW-40 Ti swing bucket rotor and centrifuged at 4°C for 16 h at 40,000 × r.p.m. Fractions (0.5 ml) were collected and used in gel electrophoresis and subsequent western blotting analyses. Western blot of the complex subunits were developed in the same films under the same exposure time for No Dox and Dox samples for proper comparison.

ChIP-seq and RNA-seq

Primary tissue was singly cross-linked using 1% formaldehyde for 10 min and cross-linking was quenched with 2.5M glycine for 5 min. Dual cross-linking was used for ChIP-seq of SWI/SNF complex subunits in cancer cell lines. Briefly, cells were first crosslinked in 2 mM disuccinimidyl glutarate (DSG; Life Technologies: Cat. #20593) for 30 min then in 1% formaldehyde for 10 min, quenched with glycine for 5 min. Cells were washed with PBS three times then used to generate nuclear extract. Chromatin was fragmented using sonication (Branson sonifier with microtip) for primary tissues or the adaptive focused acoustics (AFA) technology developed by Covaris for the cell lines. Solubilized chromatin was immunoprecipitated with antibodies against SMARCA4/BRG1 (Abcam: ab110641), SMARCC1/BAF155 (Santa Cruz: sc9746), H3K4me (Abcam: ab8895), H3K4me3 (Millipore: 07-473) and H3K27ac (Cell Signaling Technology: 8173). Antibody-chromatin complexes were pulled down with protein G-Dynabeads (Life Technologies), washed, and then eluted. After crosslinking reversal, RNase A, and proteinase K treatment, ChIP DNA was extracted with the Min-Elute PCR purification kit (Qiagen). ChIP DNA was quantified with Quant-it PicoGreen dsDNA Assay Kit (Life Technologies). 10 ng of ChIP DNA per sample was used to prepare sequencing libraries, and ChIP DNA and input controls were sequenced with the Hi-Seq Illumina genome analyzer.

For RNA-Seq, total RNA was extracted using Trizol reagent (Invitrogen) and further purified using RNeasy MinElute Cleanup Kit (Qiagen). 2 μg of total RNA was used to make the RNA-Seq library using TruSeq Total RNA Sample Prep Kit (Illumina) and sequenced with the Hi-Seq Illumina genome analyzer.

ChIP-seq processing

Alignment, fragment size estimation, and library complexity—The sequenced reads were aligned to the hg19 genome assembly using Bowtie 0.12.6[33], allowing up to 10 matches ('-m 10 --best' options). Reads on the 24 assembled chromosomes excluding the ENCODE blacklisted regions were kept for downstream analysis. Peaks of cross-correlation profiles were identified to estimate the typical fragment size for each sample. The typical fragment size for the different samples ranged between 140-180bp. Each read was considered to represent a signal at half typical fragment size from the 5′ end. Library complexity was calculated for each sample as the number of unique bp positions mapped on each strand, divided by the number of reads. For batches of experiments where the typical library complexity was below 80% (RT172, RT230, RT307, RT308, RT407), only one read mapping to each position was kept.

Identification of regions of enrichment (RoE)—Regions of enrichment (RoEs) of H3K27ac, SMARCC1, SMARCA4 ChIP-seq were called using the SPP package[34] in R, with the function get.broad.enrichment.clusters and options window.size=500 and z.thr=4, using matching input data for each sample. For H3K4me3 tracks which showed a clearer signal at promoters, the same approach was taken with z.thr=5. Overlapping SMARCA4 and SMARCC1 RoEs with z.thr=4 were used as SWI/SNF binding sites. Finally, the union of calls from NoDox and Dox conditions were calculated for each cell line. The last step reduces any bias that may arise in differential RoE calling due to thresholds. Sequencing of two input samples failed due to limited available material from primary tissues: RT307 and RT308. Input sample for RT230, which is also a brain RT was used for RoE calling in RT307 and RT308.

Classification of RoEs based on position relative to TSSs—Active TSSs in a cell type were defined as all TSSs defined in Ensembl release GRCh37.72 that overlapped an H3K4me3 peak. H3K27ac or SWI/SNF RoEs that overlapped both an H3K4me3 RoE and an active TSS were called as TSS-proximal sites. Those more than 1kb away from an H3K4me3 RoE and more than 2kb away from an active TSS were called as TSS-distal sites. The TSS-proximal H3K27ac RoEs are referred to as active promoters and the TSS-distal ones are referred to as active enhancers. Sequencing of H3K4me3 sample failed for RT308. Active TSSs for this sample were called based on the presence of strong (spp broad enrichment call with z.thr=5) H3K27ac RoEs overlapping Ensembl TSSs. Where H3K4me3 RoE calls were required in downstream analyses (TSS-distal/proximal calls, SE calling), union of H3K4me3 RoEs for the other primary rhabdoid tumor samples was substituted.

Correlation and PCA analysis of primary RT samples—Correlation analysis and principal component analysis presented in Fig. 1 and Fig. S1 were conducted using MATLAB. For H3K4me1 and H3K27ac, the read count normalized IP signal for respective modifications was calculated for each enhancer from the union of all enhancers found across represented tissues. Similarly, for H3K4me3, the read count normalized IP signal was calculated for each promoter from the union of all promoters identified across all represented tissues. Pearson linear correlation coefficients were calculated using the corrcoef function, and principal component analysis utilized the pca function.

Clustering of primary RT sample enhancers—For the heatmap in Figure 1d, Cluster 3.0[35] was used to perform k-means clustering with Euclidean distance metric and Java TreeView[36] was used for visualization. The H3K27ac signal in the heatmap represents the IP signal minus input for a +/− 1500bp window around the peak signal of each enhancer. Clusters of enhancers specific to brain-, kidney-, soft tissue-derived RTs were then combined for gene ontology analysis.

IP efficiency correction for H3K27ac samples—The efficacy of IP pulldown may vary between different ChIP-seq experiments. A number of lines of evidence suggested that the real levels of H3K27ac are unchanged at a large proportion of promoters upon SMARCB1 re-expression: i. we found that a large portion of promoters show the same amount of fold-change with very small variance; ii. the typical fold-change was independent of SWI/SNF binding at promoters, and was the same as at enhancers with no SWI/SNF binding; iii. in an accompanying study with mouse embryonic fibroblasts, we observed different average fold-change trends at promoters, both greater that and close to one-fold for replicates of experiments upon *Smarcb1* knockout, while we saw consistent decrease of H3K27ac in western blots and at enhancers. Based on these observations, we applied a small multiplicative factor on H3K27ac samples to set the mode of the log-fold-change distribution at promoters to zero while comparing Dox and NoDox samples. These factors were G401 NoDox: 1.15, Dox: 0.86; BT16 NoDox: 1.11, Dox: 0.9; TTC549: Dox/NoDox: 1.00. This normalization procedure does not affect the qualitative observations presented. We refrained from applying a similar normalization for other ChIP-seq sample pairs, since we could not confidently determine a set of regions where they are unaffected upon SMARCB1 re-expression.

Classification of RoEs based on differences between conditions—Changes in TSS-distal SWI/SNF binding upon SMARCB1 re-expression were evaluated at each RoE, by dividing the library-size normalized IP signal for SMARCC1and SMARCB1 in Dox condition by NoDox. If the geometric mean of change was greater than 1.5 fold, and both factors showed increased signal, the RoE was called as “gained/strengthened”. In reverse, if the geometric mean of change was less than 2/3 fold, and both factors showed decreased signal, the RoE was called as “lost/weakened”. Other sites were called as “unchanged”. The sites that were called in NoDox, or those where the average SMARCB1+SMARCB1 signal in NoDox was more than half the signal in Dox were considered as SWI/SNF binding sites in NoDox (used in Fig. 4a, left). The complementary selection was performed for SWI/SNF binding sites in Dox (used in Fig. 4a, right).

ChIP-seq visualization—Genomic profiles for visualization were generated using a sigma=100bp Gaussian smoothing after library size normalization (e.g. in Figures 4c,d, or output wig files). The heatmaps in Figure 4c were centered at the position with highest signal in the smoothed profile obtained by summing the four tracks considered, No-Dox SMARCC1, No-Dox SMARCA4, Dox SMARCC1, and Dox SMARCA4. The heatmaps show input subtracted values, whereas the browser shots show raw smoothed signal. The average profiles for each class in Figure 4c (e.g. stable) were obtained as 0.1–0.9 trimmed

linear mean at each position. Scatter plots in Figure 4b and 5b were obtained as (total IP signal in RoE per million mapped reads + pseudocount of 0.1)/(matching input +0.1).

Identification of super-enhancers—Super-enhancers were identified with a slightly modified approach from the original method[17]. H3K27ac RoEs were called as described above. We did not remove TSS-proximal peaks, but stitched all RoEs within 12.5kb. For each stitched RoE, instead of removing false positives from stitched enhancer peaks that encompassed active TSSs, IP and input signal were calculated only in portions that did not intersect H3K4me3 RoEs. This approach excludes high H3K27ac signal found at active promoters, while still allowing enhancers on either side of a promoter to be stitched. Each super-enhancer was associated to the closest active TSS, as defined above, within 300kb. If more than one gene is similarly close to a super-enhancer (at most 50kb further than the closest gene), those genes are also listed in the super-enhancer associated gene list.

Gene ontology analysis of enhancers with increased SWI/SNF binding—GO analysis for SMARCB1-dependent SWI/SNF enhancers was performed as follows: Gene Ontology databases were downloaded from geneontology.org on 2014/04/29. Each enhancer was associated to the closest active TSS within 100kb and within conserved topology associated domains. The p-values for gene set enrichment for genes associated to enhancers overlapping a gained/strengthended SWI/SNF RoE were calculated relative to genes associated with any enhancer using hypergeometric test. The q-values were obtained based on Benjamini–Hochberg procedure. Top 5 terms and selected developmental terms are displayed in the figures.

RNA-seq processing

Initial processing—The sequenced reads from each sample were aligned to the human genome+transcriptome assembly GRCh37.72 using TopHat v2.0.8[37] with default parameters except turning off novel junction search (-G <gtf> --no-novel-juncs). The transcriptome was self-merged to allow processing with cufflinks v2.1.1 tool cuffdiff[38], “cuffcompare -s hg19.fa -CG -r GRCh37.72.gtf GRCh37.72.gtf”. Different conditions for a given cell line were compared using cuffdiff with default parameters and bias correction (-G <gtf> -b options).

Relating RNA-seq changes to ChIP-seq changes—Each SWI/SNF or H3K27ac RoE was associated to the closest active TSS as defined above. The connection between ChIP-seq signal change and RNA-seq change was studied for TSS-proximal and TSS-distal RoEs separately. Only RoEs for which the closest active TSS is between 5kb and 100kb are retained for the TSS-distal analysis. IP signal change was quantified as ‘total IP signal in RoE per million mapped reads + pseudocount of 0.1.’ RNA signal change was quantified as ‘normalized gene level count value from cuffdiff + 5’. The ratio of IP signal for Dox sample divided by NoDox sample was used to categorize RoEs to four groups: more than 3-fold signal gain, between 1.5 to 3-fold signal gain, less than 1.5-fold change, and more than 1.5-fold signal loss. The ratio of RNA-seq signal for Dox divided by NoDox was plotted for each category.

Gene set enrichment analysis—GSEA analysis[39] was performed based on p-value for gene expression changes output by cufflinks. The weights were set as -log(p) for upregulated genes and log(p) for downregulated genes. gsea2-2.0.13.jar was run with recommended parameters.

Clustering of genes and gene ontology analysis—The heatmap for RNA-seq results (Figure S4) shows log2(fold change) values for 2171 genes, where the replicate experiment sets were considered separately. The fold change values were calculated as (normalized gene level count value from cuffdiff + 5) for Dox divided by NoDox. Genes were selected based on two requirements: having more than two fold change in at least two of the sample pairs and there being more than 50 normalized reads mapping to the gene in at least two of the samples. The samples were k-mean clustered to 10 clusters using the R function heatmap using Pearson correlation between samples (1-r) as distance metric. GO analysis was performed for each cluster separately as follows: Gene Ontology databases were downloaded from geneontology.org on 2014/04/29. All the genes for which more than 50 normalized reads map to the gene in at least two of the samples were used as background. p-value for enrichment was calculated using hypergeometric test. q-values were obtained based on Benjamini–Hochberg procedure. Selected GO terms are displayed on the figure including any term with q<1e-4, or developmental terms with q<1e-2.

Statistical analysis

All *in vitro* experiments were performed in triplicate (cell culture) unless specifically stated in figure legends, with mean and s.d. reported, $P < 0.05$ was considered significant: $*P < 0.05$, $**P < 0.001$ unless specifically stated in figures or figure legends. All gene ontology enrichment analyses were performed using hypergeometric test and multi-test corrected using Benjamini & Hochberg method [R functions phyper(lower.tail=F), p.adjust(method="BH")]. Comparison of gene expression changes for genes near different enhancer classes was performed using two sided t test. [R function t.test]. Exact p and q(FDR) values are reported for both.

Supplementary Material

Refer to Web version on PubMed Central for supplementary material.

Acknowledgments

We thank members of the Roberts and Park laboratories for assistance and discussion. We thank J. Francois (Department of Neurology, Boston Children's Hospital), J. Roth (Cancer Cytogenetics Laboratory, Children's Hospital of Philadelphia), and J. Silterra (Broad Institute) for their help in acquiring and preliminary clinical analysis of primary tumor samples; R. Rubio (Center for Cancer Computational Biology, Dana-Farber Cancer Institute) and M. Uziel (Epigenomics Program, Broad Institute) for their assistance in sequencing samples; N. Shoresh (Epigenomics Program, Broad Institute) for assistance in accessing Roadmap Epigenomics data; and R. Tomaino (Taplin Biological Mass Spectrometry Facility, Harvard Medical School) for assistance in proteomic analysis. X.W. was supported by the Pathway to Independence Award from the US National Institutes of Health (K99CA197640), a postdoctoral fellowship from the Rally Foundation for Childhood Cancer Research and The Truth 365, and a research grant from the St. Baldrick's Foundation. R.S.L. was partially supported by an NSF Graduate Research Fellowship. This work was supported by US National Institutes of Health grants R01CA172152 (C.W.M.R.), R01CA113794 (C.W.M.R.) and U54 HG006991 (B.E.B). The Avalanna Fund, the Cure AT/RT Now foundation, the Garrett B. Smith Foundation, Miles for Mary and ALSAC/St. Jude (C.W.M.R.) provided additional support.

References

1. Wilson BG, Roberts CWM. SWI/SNF nucleosome remodellers and cancer. Nat RevCancer. 2011; 11:481–92.
2. Wu JI, Lessard J, Crabtree GR. Understanding the words of chromatin regulation. Cell. 2009; 136:200–6. [PubMed: 19167321]
3. Biegel JA, et al. Germ-line and acquired mutations of INI1 in atypical teratoid and rhabdoid tumors. Cancer Res. 1999; 59:74–9. [PubMed: 9892189]
4. Versteege I, et al. Truncating mutations of hSNF5/INI1 in aggressive paediatric cancer. Nature. 1998; 394:203–6. [PubMed: 9671307]
5. Eaton KW, Tooke LS, Wainwright LM, Judkins AR, Biegel JA. Spectrum of SMARCB1/INI1 mutations in familial and sporadic rhabdoid tumors. Pediatr Blood Cancer. 2011; 56:7–15. [PubMed: 21108436]
6. Lee RS, et al. A remarkably simple genome underlies highly malignant pediatric rhabdoid cancers. J Clin Invest. 2012; 122:2983–8. [PubMed: 22797305]
7. Hasselblatt M, et al. High-resolution genomic analysis suggests the absence of recurrent genomic alterations other than SMARCB1 aberrations in atypical teratoid/rhabdoid tumors. Genes Chromosomes Cancer. 2013; 52:185–90. [PubMed: 23074045]
8. Lawrence MS, et al. Mutational heterogeneity in cancer and the search for new cancer-associated genes. Nature. 2013; 499:214–8. [PubMed: 23770567]
9. Stio E, Mckenna G, Ahmad K, Hahn W, Walter J. Characterization of the Tumor Suppressor Mechanism of SNF5 Advisor: Charles Roberts. 2009
10. Zhou VW, Goren A, Bernstein BE. Charting histone modifications and the functional organization of mammalian genomes. Nat Rev Genet. 2011; 12:7–18. [PubMed: 21116306]
11. Zhu J, et al. Genome-wide chromatin state transitions associated with developmental and environmental cues. Cell. 2013; 152:642–54. [PubMed: 23333102]
12. Consortium R. E. et al. Integrative analysis of 111 reference human epigenomes. Nature. 2015; 518:317–330. [PubMed: 25693563]
13. Chun HJE, et al. Genome-Wide Profiles of Extra-cranial Malignant Rhabdoid Tumors Reveal Heterogeneity and Dysregulated Developmental Pathways. Cancer Cell. 2016; 29:394–406. [PubMed: 26977886]
14. Johann PD, et al. Atypical Teratoid/Rhabdoid Tumors Are Comprised of Three Epigenetic Subgroups with Distinct Enhancer Landscapes. Cancer Cell. 2016; 29:379–93. [PubMed: 26923874]
15. Wang S, et al. Target analysis by integration of transcriptome and ChIP-seq data with BETA. Nat Protoc. 2013; 8:2502–2515. [PubMed: 24263090]
16. Stappenbeck TS, Miyoshi H. The role of stromal stem cells in tissue regeneration and wound repair. Science. 2009; 324:1666–9. [PubMed: 19556498]
17. Whyte, Wa, et al. Master transcription factors and mediator establish super-enhancers at key cell identity genes. Cell. 2013; 153:307–19. [PubMed: 23582322]
18. Hnisz D, et al. Super-enhancers in the control of cell identity and disease. Cell. 2013; 155:934–47. [PubMed: 24119843]
19. Bergsland M, et al. Sequentially acting Sox transcription factors in neural lineage development. Genes Dev. 2011; 25:2453–64. [PubMed: 22085726]
20. Yu H, et al. Frizzled 1 and frizzled 2 genes function in palate, ventricular septum and neural tube closure: general implications for tissue fusion processes. Development. 2010; 137:3707–17. [PubMed: 20940229]
21. Abrahams A, Parker MI, Prince S. The T-box transcription factor Tbx2: its role in development and possible implication in cancer. IUBMB Life. 2010; 62:92–102. [PubMed: 19960541]
22. Wang X, et al. Oncogenesis caused by loss of the SNF5 tumor suppressor is dependent on activity of BRG1, the ATPase of the SWI/SNF chromatin remodeling complex. Cancer Res. 2009; 69:8094–101. [PubMed: 19789351]

23. Isakoff MS, et al. Inactivation of the Snf5 tumor suppressor stimulates cell cycle progression and cooperates with p53 loss in oncogenic transformation. Proc Natl Acad Sci U S A. 2005; 102:17745–50. [PubMed: 16301525]
24. Tolstorukov MY, et al. Swi/Snf chromatin remodeling/tumor suppressor complex establishes nucleosome occupancy at target promoters. Proc Natl Acad Sci U S A. 2013; 110:10165–70. [PubMed: 23723349]
25. Yu Y, et al. Olig2 targets chromatin remodelers to enhancers to initiate oligodendrocyte differentiation. Cell. 2013; 152:248–61. [PubMed: 23332759]
26. Bossen C, et al. The chromatin remodeler Brg1 activates enhancer repertoires to establish B cell identity and modulate cell growth. Nat Immunol. 2015; 16:775–84. [PubMed: 25985234]
27. Alexander JM, et al. Brg1 modulates enhancer activation in mesoderm lineage commitment. Development. 2015; 142:1418–30. [PubMed: 25813539]
28. Doan DN, et al. Loss of the INI1 tumor suppressor does not impair the expression of multiple BRG1-dependent genes or the assembly of SWI/SNF enzymes. Oncogene. 2004; 23:3462–73. [PubMed: 14990991]
29. Lovén J, et al. Selective inhibition of tumor oncogenes by disruption of super-enhancers. Cell. 2013; 153:320–34. [PubMed: 23582323]
30. Kaur H, et al. The chromatin-modifying protein HMGA2 promotes atypical teratoid/rhabdoid cell tumorigenicity. J Neuropathol Exp Neurol. 2015; 74:177–85. [PubMed: 25575139]
31. Wang X, et al. TCR-dependent transformation of mature memory phenotype T cells in mice. J Clin Invest. 2011; 121:3834–3845. [PubMed: 21926465]
32. Helming KC, et al. ARID1B is a specific vulnerability in ARID1A-mutant cancers. Nat Med. 2014; 20:251–254. [PubMed: 24562383]
33. Langmead B, Trapnell C, Pop M, Salzberg SL. Ultrafast and memory-efficient alignment of short DNA sequences to the human genome. Genome Biol. 2009; 10:R25. [PubMed: 19261174]
34. Kharchenko PV, Tolstorukov MY, Park PJ. Design and analysis of ChIP-seq experiments for DNA-binding proteins. Nat Biotechnol. 2008; 26:1351–9. [PubMed: 19029915]
35. de Hoon MJL, Imoto S, Nolan J, Miyano S. Open source clustering software. Bioinformatics. 2004; 20:1453–4. [PubMed: 14871861]
36. Saldanha AJ. Java Treeview--extensible visualization of microarray data. Bioinformatics. 2004; 20:3246–8. [PubMed: 15180930]
37. Kim D, et al. TopHat2: accurate alignment of transcriptomes in the presence of insertions, deletions and gene fusions. Genome Biol. 2013; 14:R36. [PubMed: 23618408]
38. Trapnell C, et al. Differential analysis of gene regulation at transcript resolution with RNA-seq. Nat Biotechnol. 2013; 31:46–53. [PubMed: 23222703]
39. Subramanian A, et al. Gene set enrichment analysis: a knowledge-based approach for interpreting genome-wide expression profiles. Proc Natl Acad Sci U S A. 2005; 102:15545–50. [PubMed: 16199517]

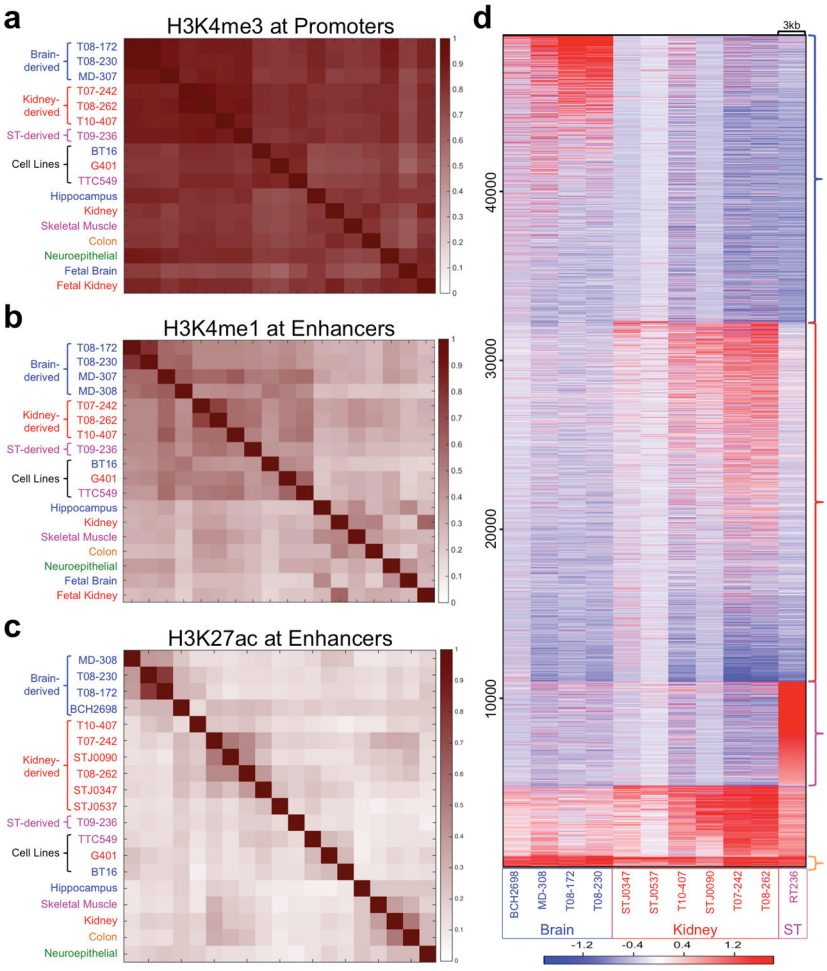

e

TermID	Term	q-value	Genes in Term	Target Genes in Term
Brain-derived RT				
GO:0010646	Regulation of Cell Communication	1.51E-09	2533	210
GO:0006928	Cellular Component Movement	1.29E-08	1227	119
GO:0022008	Neurogenesis	6.86E-08	1284	120
GO:0048468	Cell Development	7.86E-08	1370	125
GO:0009653	Anatomical Structure Morphogenesis	2.94E-07	1946	160
Kidney-derived RT				
GO:0048583	Regulation Of Response To Stimulus	2.67E-18	2937	266
GO:0009966	Regulation of Signal Transduction	5.47E-15	2269	211
GO:0002376	Immune System Process	2.07E-12	1892	176
GO:0009611	Response to Wounding	3.20E-13	1005	112
GO:0051174	Regulation of Phosphorus Metabolic Process	1.48E-10	1772	161
Soft tissue-derived RT				
GO:0051056	Regulation of Small GTPase Mediated Signal Transduction	6.99E-06	480	47
GO:0046578	Regulation Of Ras Protein Signal Transduction	9.39E-05	406	39
GO:0032502	Developmental Process	1.04E-04	4647	234
GO:0009653	Anatomical Structure Morphogenesis	1.04E-04	1946	116
GO:0009894	Regulation of Catabolic Process	1.34E-04	869	63
Shared by RT				
GO:0032502	Developmental Process	2.49E-07	4647	145
GO:0048856	Anatomical Structure Development	6.31E-07	4089	130

f

Brain RT							Kidney RT
ADAMTS3	EYA2	GALNT10	MMP24	PARD3B	REPIN1	SPRY1	ANGPT1
ATF1	FAM107A	GJA1	MSI2	PAXBP1	RFX3	TFPI	CBX3
CASK	FAM19A3	GLIS3	MYO10	PPP4R2	RHOH	TMED10	DAAM1
CCDC41	FAM65B	GPR98	NLGN1	PRDM16	RMST	TMEM164	DNM3
CDCP1	FAM84B	HAAO	NPAS3	PYGO1	RPA3	USP11	MCTP2
CHKA	FAM95B1	KCNE1/2	NUAK2	QKI	RPS6KA2	USP3	MEIS1
CITED2	FGFBP3	LHFP	NWD1	RAB11FIP1	RPS6KA5	VPS53	PSMD7
CUEDC1	FZD1	MACF1	NXN	RAG1/2	SHROOM3		RERG
DST	FZD3	MITF	OTX2	RAI1	SOX2		TBX2

Figure 1. Histone modification landscape in primary rhabdoid tumors and cell lines

Rhabdoid tumors from different tissues show commonalities in H3K4me1 or H3K4me3 signal, but are clearly distinct in terms H3K27ac signal at enhancers.

a. Pearson correlations of H3K4me3 signal at the union of all promoters.

b. Pearson correlations of H3K4me1 signal at the union of all enhancers.

c. Pearson correlations of H3K27ac signal at the union of all enhancers.

d. K-means clustering of H3K27ac signal at loci called as enhancers. Brain-derived rhabdoid tumor (blue), kidney-derived rhabdoid tumor (red), and soft tissue-derived rhabdoid tumor (purple) all had enhancers unique to each respective tissue.

e. Selected terms from gene ontology analyses of the nearest genes to the top 2000 enhancers found in each cluster in (**d**) with a full list of top gene ontology terms in Supplementary Table 1.

f. SE associated genes common across and specific to brain or kidney rhabdoid tumors. Genes putatively involved in the developmental processes of these respective tissues are bolded and in color.

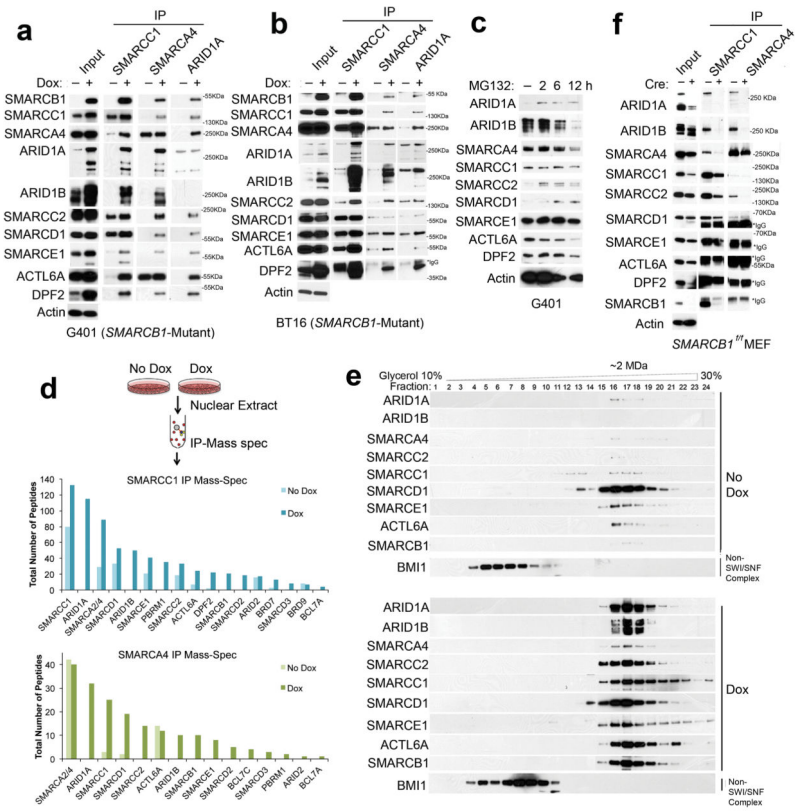

Figure 2. SMARCB1 is essential in maintaining the SWI/SNF complex integrity

a–b. Immunoprecipitation (IP) of the SWI/SNF complex subunits SMARCC1, SMARCA4, or ARID1A from the nuclear extracts of G401 (**a**) and BT16 (**b**) cell lines with or without Doxycycline (Dox)-induced *SMARCB1* re-expression. Immunoblotted for subunits SMARCB1, SMARCC1, SMARCA4, ARID1A, ARID1B, SMARCC2, SMARCD1, SMARCE1, ACTL6A, and DPF2. Actin is a loading control.

c. Mass spectrometry showing increased recovered peptides of SWI/SNF complex subunits by IP of SMARCA4 and SMARCC1 in G401 cells after *SMARCB1* re-expression (Dox vs. No Dox).

d. Glycerol sedimentation (10–30%) assay of SWI/SNF complex (~2MDa) from *SMARCB1*-deficient G401 cells without (top half) or with Dox (bottom half) immunoblotted for the indicated SWI/SNF complex subunits. BMI1 is a PRC1 complex subunit serving as a control.

e. Immunoprecipitation (IP) of the SWI/SNF complex by SMARCC1 or SMARCA4 from the nuclear extracts of WT or *Smarcb1* deficient mouse embryonic fibroblasts immunoblotted for the indicated SWI/SNF complex subunits.

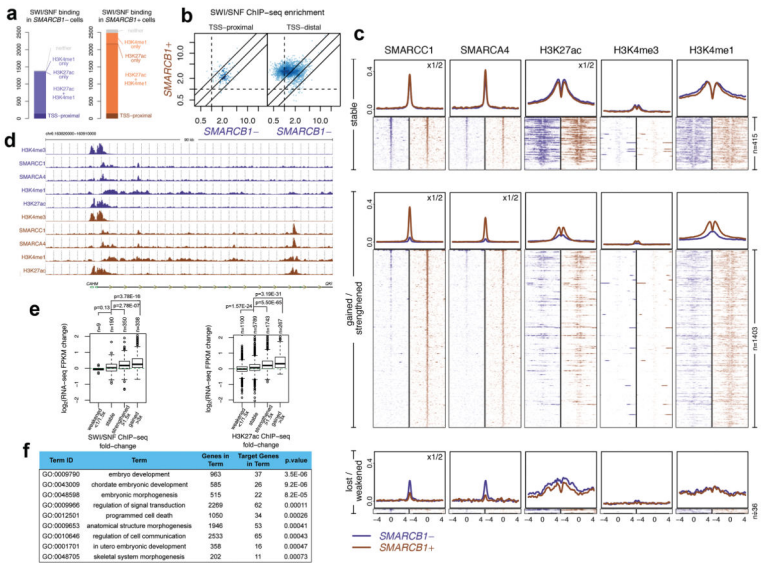

Figure 3. *SMARCB1* re-expression alters the SWI/SNF complex targeting at typical enhancers

a. Number of SWI/SNF (SMARCC1 and SMARCA4) binding sites in regions of enrichment of different histone marks in G401 cells without or with *SMARCB1* re-expression.

b. Average enrichment of SMARCC1 and SMARCA4 without vs. with *SMARCB1* re-expression in TSS-distal or TSS-proximal SWI/SNF binding sites.

c. Heatmaps depicting SMARCC1, SMARCA4, H3K27ac, H3K4me1, and H3K4me3 signal intensities for TSS-distal SWI/SNF binding sites, grouped by change upon *SMARCB1* re-expression. The rows show 9 kb regions, centered on SMARCC1/SMARCA4 peaks, ranked by overall signal intensities of SMARCC1/SMARCA4. Average profiles for each heatmap is shown above, where different y-axis ranges are denoted as 1/2x or 1/4x.

d. Representative screenshot of SMARCC1, SMARCA4, H3K4me1, H3K4me3, and H3K27Ac signal without or with *SMARCB1* re-expression in G401 cells showing increased SMARCC1/SMARCA4 binding upon *SMARCB1* re-expression accompanied with increased and flanking H3K27ac and H3K4me1 marks at enhancers.

e. Correlation of gene expression changes with SMARCC1/SMARCA4 binding or H3K27ac signal at TSS-distal binding sites in G401 cells upon Dox treatment.

f. Gene Ontology (GO) analysis of genes proximal to enhancers with increased SMARCC1/SMARCA4 signal upon Dox treatment.

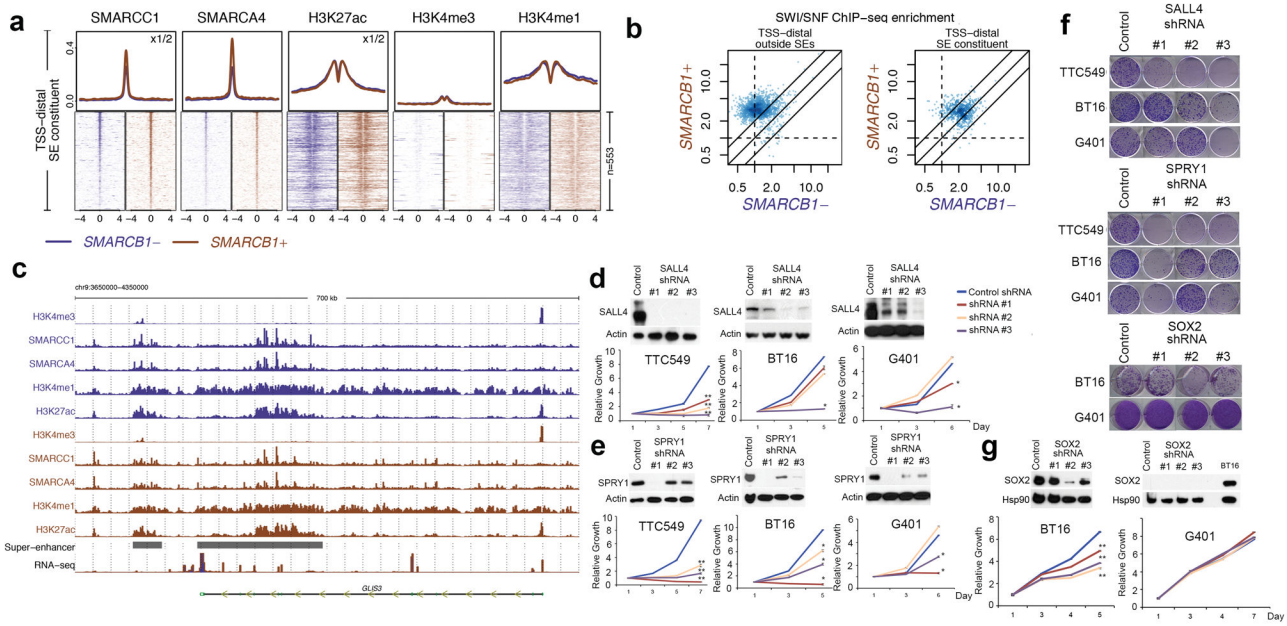

Figure 4. Residual SWI/SNF complexes are specifically maintained at super-enhancers in *SMARCB1*-deficient rhabdoid tumors

a. Heatmaps depicting SMARCC1, SMARCA4, H3K27ac, H3K4me1, and H3K4me3 signal intensities for SMARCC1/SMARCA4 bound within super-enhancers.

b. Scatter plots showing change of average SMARCC1/SMARCA4 signal for TSS-proximal binding sites or TSS-distal ones split to outside and inside super-enhancers.

c. Representative screenshot in G401 cells showing limited changes SMARCC1, SMARCA4, H3K27ac, or H3K4me1 upon SMARCB1 re-expression inside super-enhancers, in contrast to outside.

d–g. Knockdown of *SALL4* (**d**) or *SPRY1* (**e**) in G401, BT16, and TTC549 cells affects cell proliferation and colony forming abilities (**f**), while knockdown of *SOX2* only affect the proliferation and colony forming abilities of BT16 but not G401 cells (**g** and **f**). Error bar means s.d.; **: $P < 0.001$; *: $P < 0.05$ (t-test, two-side; n=3)

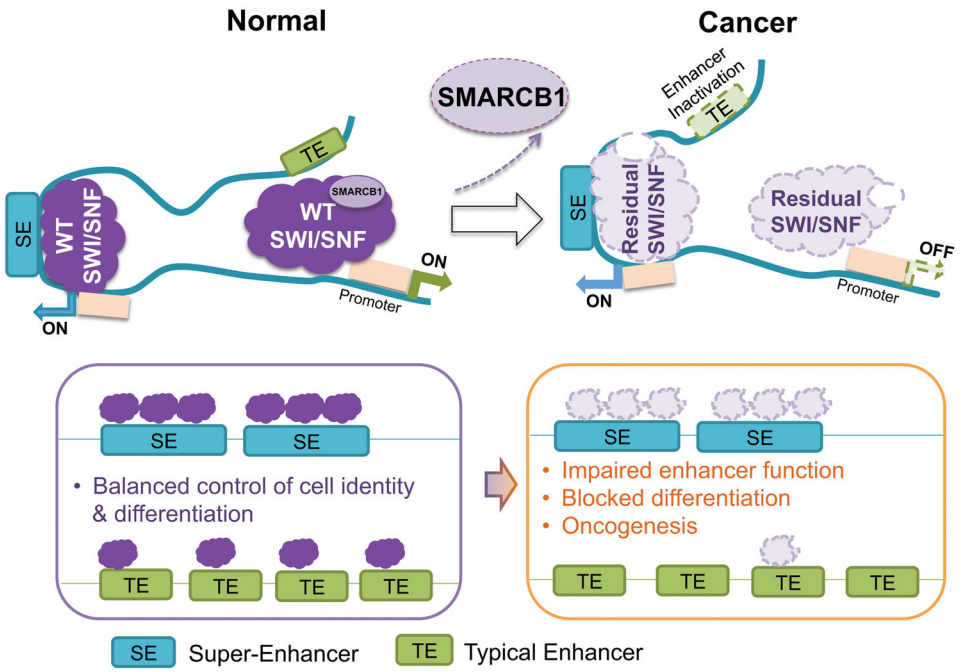

Figure 5. Working model

SMARCB1 functions to stabilize the SWI/SNF complex, thus enabling it to bind and facilitate enhancer formation and function. Loss of SMARCB1 results in markedly reduced levels of the SWI/SNF complex, which results in reduced genome-wide targeting at regular enhancers thus impairing their functions. However, the small amount of residual SWI/SNF complex preferentially present at super-enhancers is key to the maintenance of aberrant cell identity.